References

Bintanja, R. and van de Wal, R. S. W.: North American ice-sheet dynamics and the onset of the 100,000-year glacial cycles, Nature, 454, 869–872, https://doi.org/10.1038/nature07158, 2008.

EPICA-community-members: Eight glacial cycles from an Antarctic ice core, Nature, 429, 623–628, https://doi.org/10.1038/nature02599, 2004.

Flower, B. P., Oppo, D. W., McManus, J. F., Venz, K. A., Hodell, D. A., and Cullen, J. L.: North Atlantic intermediate to deep water circulation and chemical stratification during the past 1 Myr, Paleoceanography, 15, 388–403, https://doi.org/10.1029/1999PA000430, 2000.

Jouzel, J., Masson-Delmotte, V., Cattani, O., Dreyfus, G., Falourd, S., Hoffmann, G., Minster, B., Nouet, J., Barnola, J. M., Chappellaz, J., Fischer, H., Gallet, J. C., Johnsen, S., Leuenberger, M., Loulergue, L., Luethi, D., Oerter, H., Parrenin, F., Raisbeck, G., Raynaud, D., Schilt, A., Schwander, J., Selmo, E., Souchez, R., Spahni, R., Stauffer, B., Steffensen, J. P., Stenni, B., Stocker, T. F., Tison, J. L., Werner, M., and Wolff, E. W.: Orbital and millennial Antarctic climate variability over the last 800 000 years, Science, 317, 793–796, https://doi.org/10.1126/science.1141038, 2007.

Köhler, P. and Munhoven, G.: Late Pleistocene carbon cycle revisited by considering solid Earth processes, Paleoceanography and Paleoclimatology, 35, e2020PA004 020, https://doi.org/10.1029/2020PA004020, 2020.

Köhler, P., Fischer, H., Munhoven, G., and Zeebe, R. E.: Quantitative interpretation of atmospheric carbon records over the last glacial termination, Global Biogeochemical Cycles, 19, GB4020, https://doi.org/10.1029/2004GB002345, 2005.

Lambert, F., Delmonte, B., Petit, J. R., Bigler, M., Kaufmann, P. R., Hutterli, M. A., Stocker, T. F., Ruth, U., Steffensen, J. P., and Maggi, V.: Dust-climate couplings over the past 800,000 years from the EPICA Dome C ice core, Nature, 452, 616–619, https://doi.org/10.1038/nature06763, 2008.

Lisiecki, L. E.: Atlantic overturning responses to obliquity and precession over the last 3 Myr, Paleoceanography, 29, 71–86, https://doi.org/10.1002/2013PA002505, 2014.

Lisiecki, L. E. and Stern, J. V.: Regional and global benthic δ^{18}O stacks for the last glacial cycle, Paleoceanography, 31, 1368–1394, https://doi.org/10.1002/2016PA003002, 2016.

McManus, J. F., Oppo, D. W., and Cullen, J. L.: A 0.5-million-year record of millennial-scale climate variability in the North Atlantic, Science, 283, 971–975, https://doi.org/10.1126/science.283.5404.971, 1999.

Wright, A. K. and Flower, B. P.: Surface and deep ocean circulation in the subpolar North Atlantic during the mid-Pleistocene revolution, Paleoceanography, 17, 1068, https://doi.org/10.1029/2002PA000782, 2002.

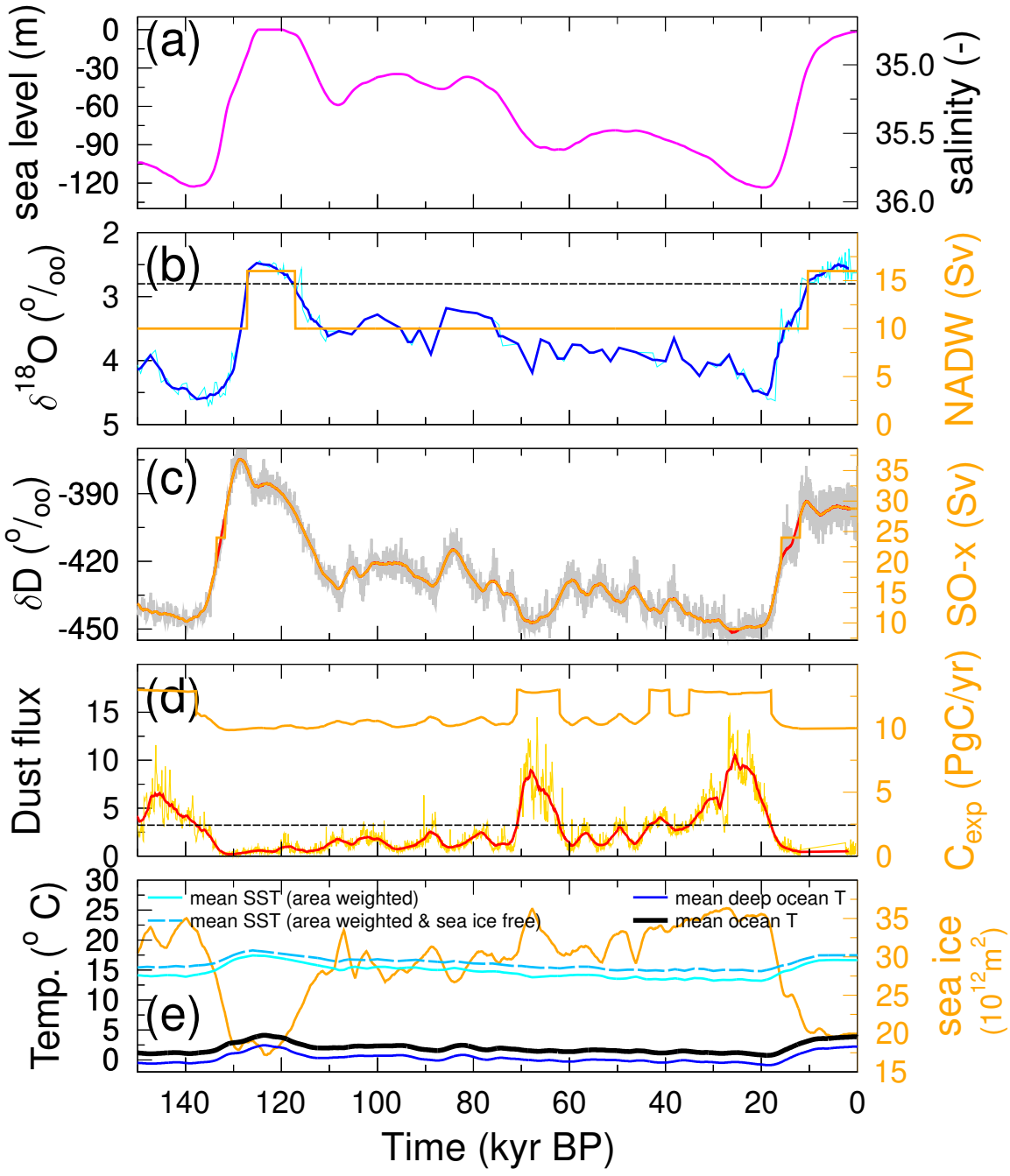

Figure S1. Time-dependent forcing of the model, adapted from Köhler and Munhoven (2020). (a) Sea level following Bintanja and van de Wal (2008) resulting of corresponding mean ocean salinity (right y-axis). (b) North Atlantic Deep Water (NADW) formation is either in interglacial or glacial mode, following $\delta^{18}O$ in OPD980 (55°29′ N, 14°42′ W) (McManus et al., 1999; Flower et al., 2000; Wright and Flower, 2002), dotted line marks the threshold for switching between both states. (c) EDC ice core δD (EPICA-community-members, 2004; Jouzel et al., 2007) corrected for $\delta^{18}O_{sw}$, from which Southern Ocean sea surface temperatures (SST) and vertical mixing (SO-x: SO surface-to-deep ocean flux, right y-axis) is calculated. The running mean of the corrected δD and SO-x differ during terminations, since abrupt changes in SO-x have been proposed (Köhler et al., 2005). Furthermore, a minimum for SO-x of 9 Sv is prescribed leading to small differences between long-term forcing and SO-x around 27 kyr BP. (d) Marine biology in the Southern Ocean (SO) is either Fe-limited or Fe-unlimited following dust fluxes in the EDC ice core (Lambert et al., 2008). The dotted line marks the threshold for switching between both states, leading to global integrated export production of organic matter at 100 m water depth (right y-axis). (e) Different ocean temperatures averaged within the model. SST is calculated from all ocean surface boxes, deep ocean temperature from the boxes with water depths below 1 km. The SST in the sea ice free area is relevant for air-sea gas exchange. Right y-axis: global integrated sea ice area. In subfigures b–d original data (thin lines) and 3-kyr-running mean (bold lines) are shown. BICYCLE is forced by the running-mean data.

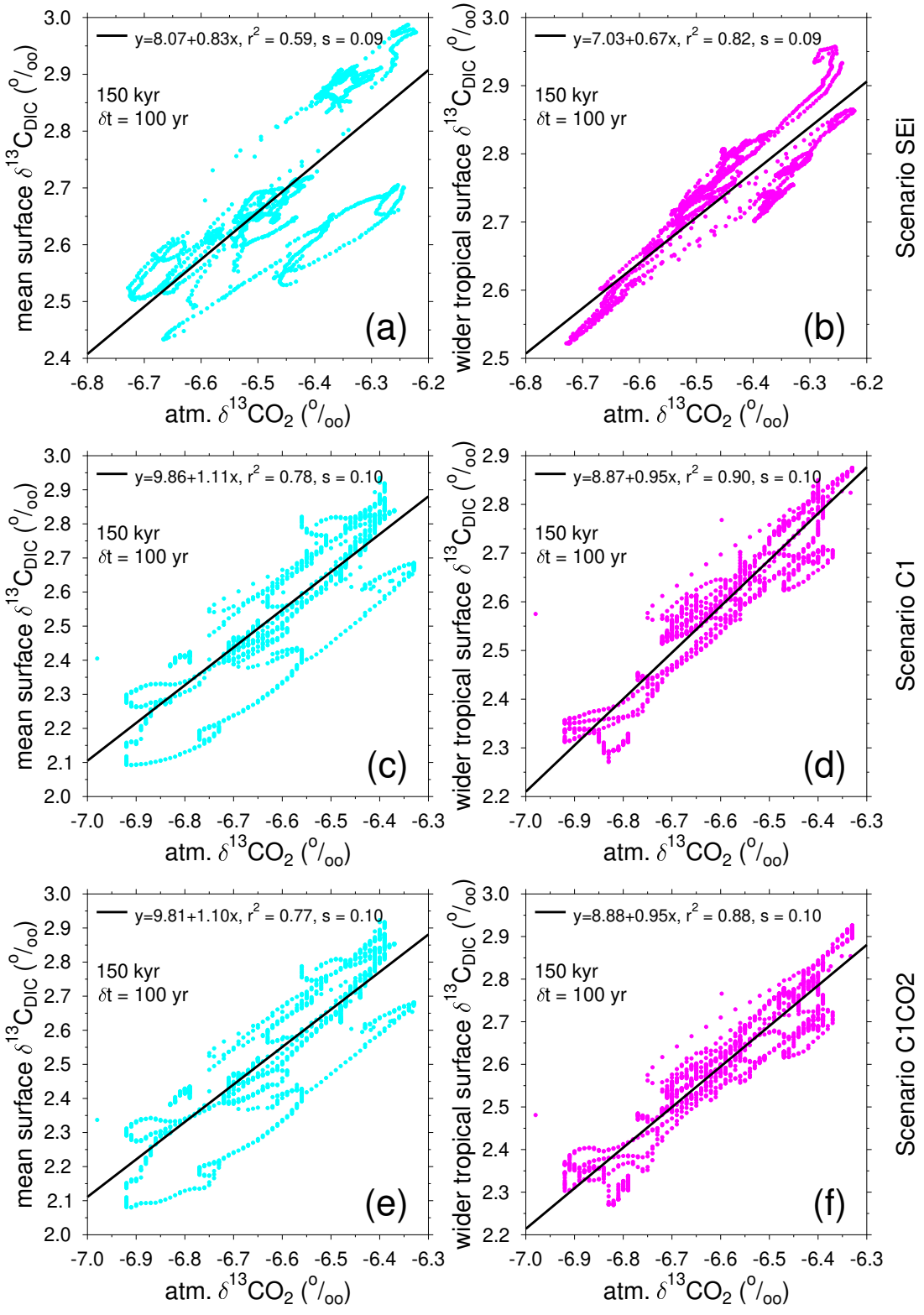

Figure S2. Scatter plots between atmospheric $\delta^{13}CO_2$ and surface ocean $\delta^{13}C_{DIC}$ (a,c,d: global area mean; b,d,f: wider tropics only) for scenarios SEi (a,b), C1 (c,d), C1CO2 (e,f) during the last 150 kyr of the simulations. The root-mean-square-error is depicted by s.

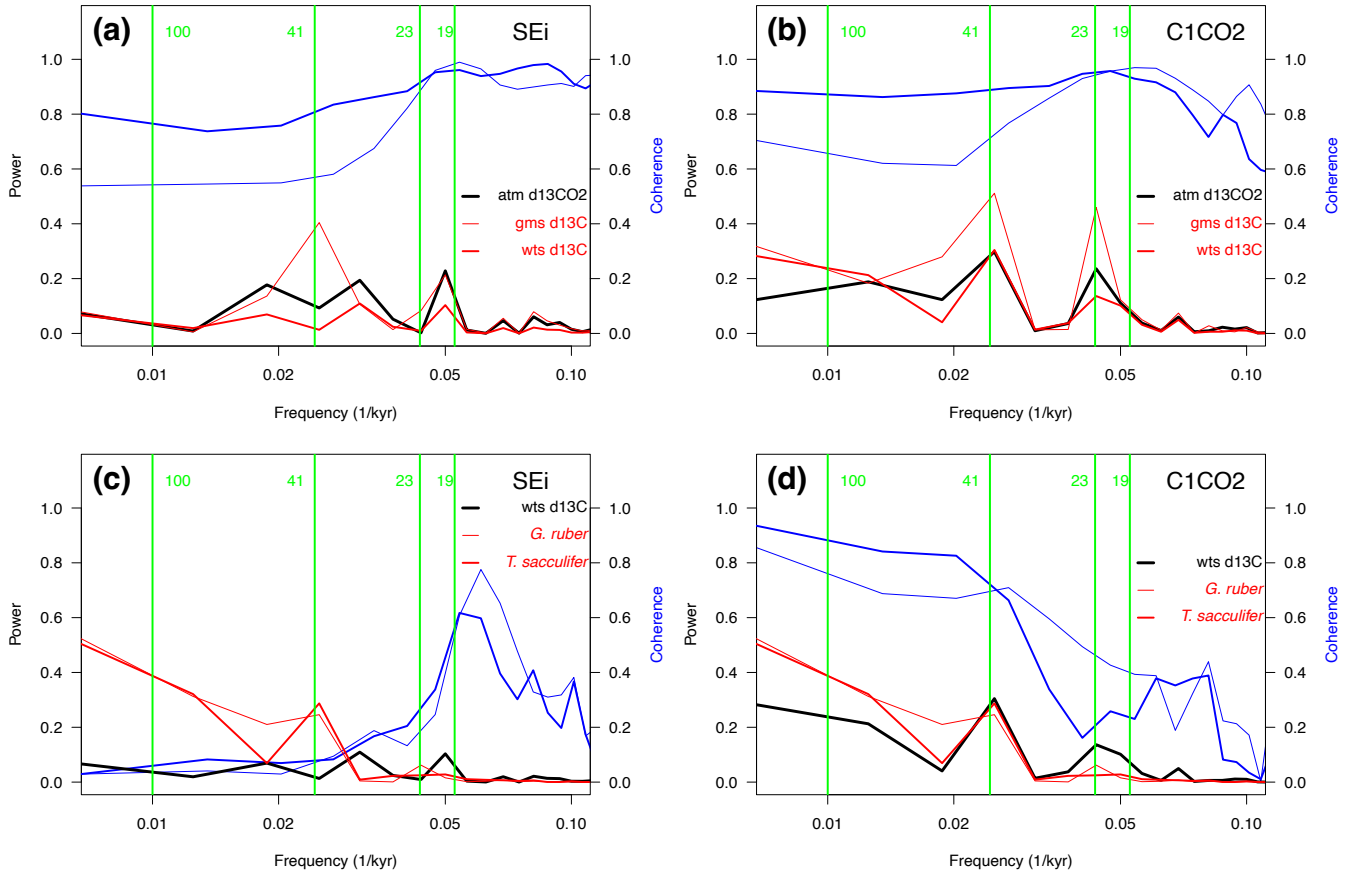

Figure S3. Frequency and coherence analysis of δ^{13}C time series from our new data stacks (c,d) and simulation scenarios (a,c) SEi and (b,d) C1CO2. Power in frequencies is calculated (a,b) for atmospheric (atm) $\delta^{13}CO_2$, global mean surface (gms) δ^{13}C and wider tropical surface (wts) δ^{13}C, or (c,d) for wts δ^{13}C and our new δ^{13}C stacks based on either *G. ruber* ($\Delta(\delta^{13}C_{rub})$) or *T. sacculifer* ($\Delta(\delta^{13}C_{sac})$). The coherence (blue lines, right y-axis) is calculated (a,b) between atm $\delta^{13}CO_2$ and either gms δ^{13}C (thin line) or wts δ^{13}C (thick line), or (c,d) between wts δ^{13}C and either $\Delta(\delta^{13}C_{rub})$ (thin line) or $\Delta(\delta^{13}C_{sac})$ (thick line). Main orbital frequencies of 100, 41, 23 and 19-kyr are marked by vertical lines.

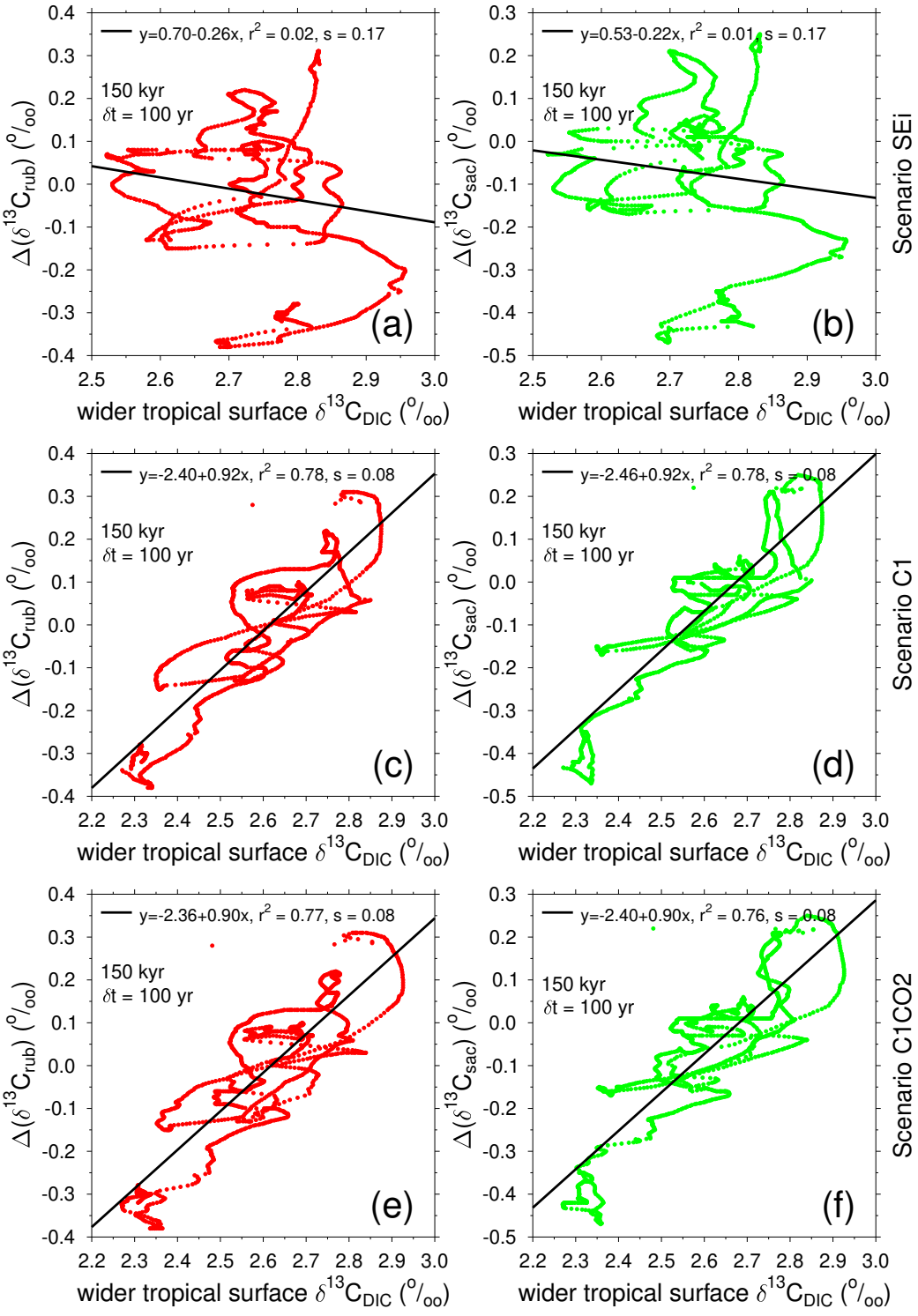

Figure S4. Scatter plots between 150 kyr simulated $\delta^{13}C_{DIC}$ in three different scenarios (a,b: SEi, c,d: C1; e,f: C1CO2) and our new mono-specific stacks (left) $\Delta(\delta^{13}C_{rub})$ and (right) $\Delta(\delta^{13}C_{sac})$. The root-mean-square-error is depicted by s.

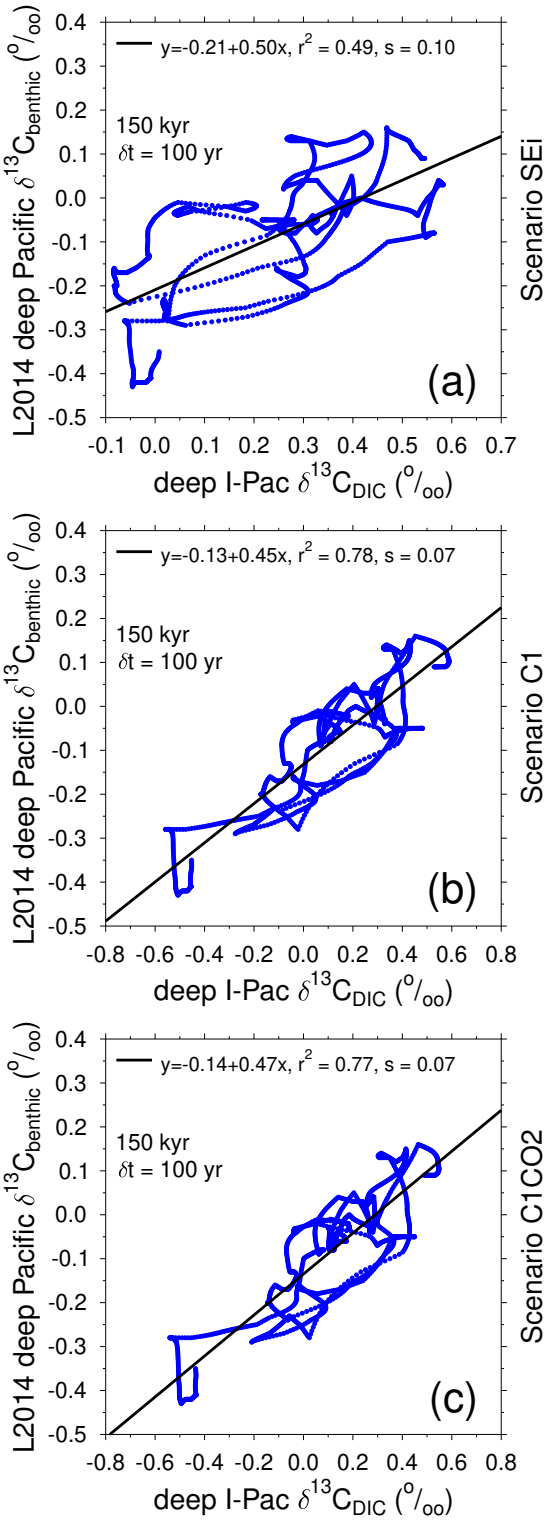

Figure S5. Scatter plots between 150 kyr simulated $\delta^{13}C_{DIC}$ in the deep Indo-Pacific in three different scenarios (a: SEi, b: C1; c: C1CO2) and a stack of deep Pacific $\delta^{13}C_{benthic}$ from Lisiecki (2014) (L2014). The root-mean-square-error is depicted by s.

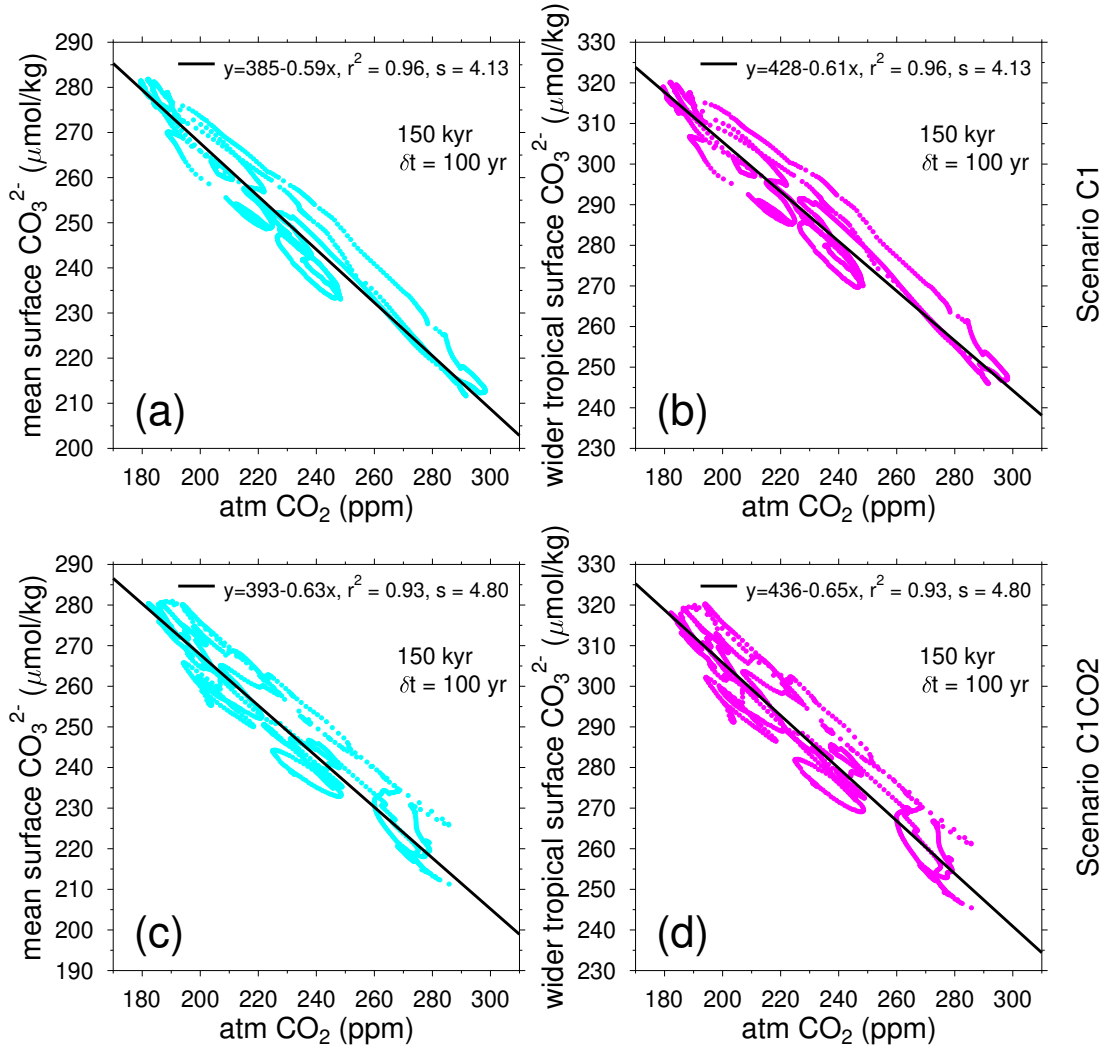

Figure S6. Scatter plots between atmospheric CO_2 and surface ocean CO_3^{2-} (a,c: global mean; b,d: wider tropics only) in scenarios (a,b) C1 and (c,d) C1CO2 for the last 150 kyr of the simulations. The root-mean-square-error is depicted by s.

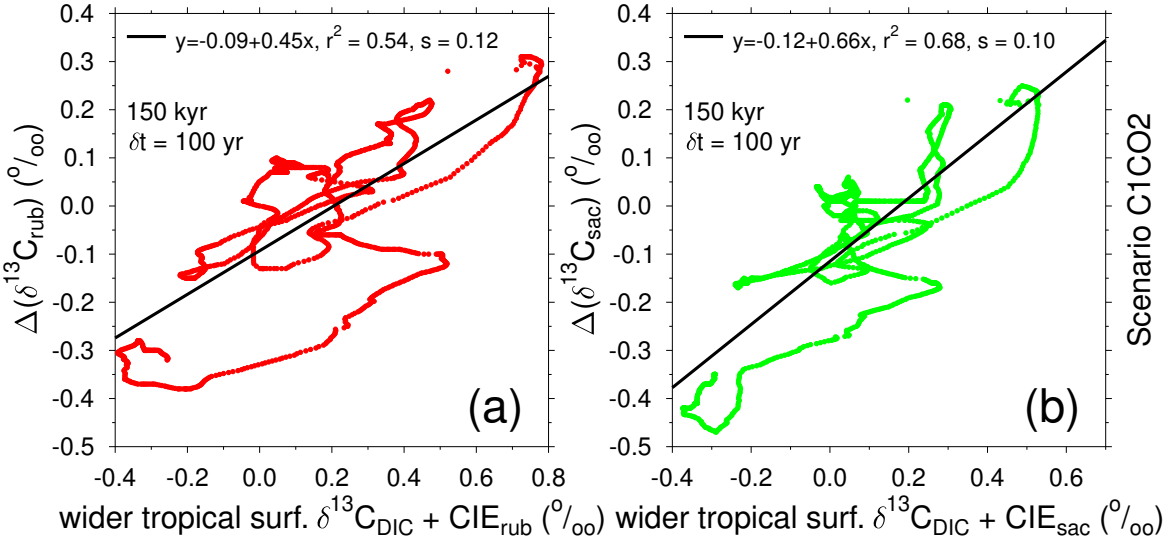

Figure S7. Scatter plots between 150 kyr simulated $\delta^{13}\mathrm{C_{DIC}}$ in scenario C1CO2 corrected by a hypothetic CIE against our new monospecific stacks (a) $\Delta(\delta^{13}\mathrm{C_{rub}})$ and (b) $\Delta(\delta^{13}\mathrm{C_{sac}})$. The root-mean-square-error is depicted by s.

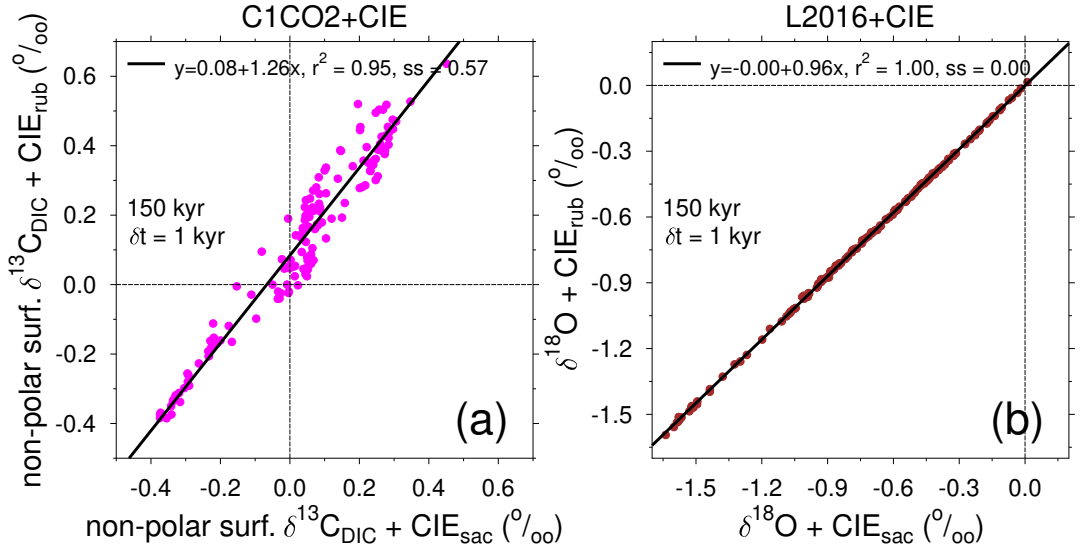

Figure S8. Scatter plot of how isotope data should be recorded in planktic foraminifera if surface ocean data are corrected for the CIE. (a) Potential $\Delta(\delta^{13}\mathrm{C_{rub}})$ (wider tropical surface ocean $\delta^{13}\mathrm{C_{DIC}}$ + CIE for *G. ruber*) versus potential $\Delta(\delta^{13}\mathrm{C_{sac}})$ (wider tropical surface ocean $\delta^{13}\mathrm{C_{DIC}}$ + CIE for *T. sacculifer*) based on 150 kyr of simulation results of scenario C1CO2 and CIE-corrections as calculated in Figure 8a–d. (b) Potential $\Delta(\delta^{18}\mathrm{O_{rub}})$ (mean ocean δ^{18}O + CIE for *G. ruber*) versus potential $\Delta(\delta^{18}\mathrm{O_{sac}})$ (mean ocean δ^{18}O + CIE for *T. sacculifer*) based on global ocean δ^{18}O as calculated in Lisiecki and Stern (2016) (L2016) and CIE-corrections as calculated in Figure 8e–h. The root-mean-square-error is depicted by s.